The micro-imaging station of the TopoTomo beamline at the ANKA synchrotron light source

A. Rack, T. Weitkamp, S. Bauer Trabelsi, P. Modregger, A. Cecilia,
T. dos Santos Rolo, T. Rack, D. Haas, R. Simon, T. Baumbach
Forschungszentrum Karlsruhe / K.I.T.,
*Institute for Synchrotron Radiation – ANKA, Germany**

R. Heldele, M. Schulz
Forschungszentrum Karlsruhe / K.I.T.,
Institute for Materials Research III, Germany

B. Mayzel
Tel Aviv University, Faculty of Life Sciences, Israel

A. N. Danilewsky
Kristallographie, Geowissenschaftliches Institut, University of Freiburg, Germany

T. Waterstradt, W. Diete
ACCEL Instruments GmbH, Bergisch Gladbach, Germany

H. Riesemeier, B. R. Müller
Bundesanstalt für Materialforschung und -prüfung,
Divisions Structure Analysis; Polymer Analysis (I.3)
and Radiological Methods (VIII.3), Berlin, Germany

(Dated: April 7, 2009)

Abstract

The TopoTomo bending magnet beamline at the ANKA synchrotron facility in Karlsruhe (Germany) operates in the hard X-ray regime (above 6 keV). Recently, an X-ray micro-imaging station has been installed at TopoTomo. For typical imaging applications, a filtered white beam or from 2009 on a double-multilayer monochromator is used. In order to optimize the field of view and the resolution of the available indirect pixel detectors, different optical systems have been installed, adapted, respectively, to a large field of view (macroscope) and to high spatial resolution (microscope). They can be combined with different camera systems, ranging from 14-bit dynamic range CCDs to fast CMOS cameras. The spatial resolution can be brought substantially beyond the micrometer limit by using a Bragg magnifier. Due to the moderate flux of the beamline compared to insertion-device beamlines on 3rd generation light sources, special emphasis has been put on the efficiency of the detectors via a dedicated scintillator concept. The layout of the beamline optics makes optimal use of the coherence properties. Thus, absorption contrast, phase contrast and analyzer-based imaging can be applied. Additionally, white beam synchrotron topography is performed, using digital indirect X-ray pixel detectors as well as X-ray film.

PACS numbers: 87.59.-e; 07.85.Qe; 81.70.Tx

Keywords: micro-tomography, synchrotron instrumentation, coherent imaging, X-ray phase contrast, Synchrotron-CT, scintillator, Bragg magnification, Analyzer-based imaging, X-ray topography

*Corresponding authors' current address: A. Rack / T. Weitkamp, ESRF, BP 220, 38043 Grenoble Cedex, France, tel: +33 (0)476 88 1781, fax: +33 (0)476 88 2785, e-mail: arack@snafu.de, weitkamp@esrf.fr

I. INTRODUCTION

The use of synchrotron light for hard X-ray based micro-imaging instead of X-rays from laboratory sources allows for applications requiring a high spatial resolution, high signal-to-noise ratio, different contrast modalities or ultra-short acquisition times. This is due to the high photon flux density, the quasi-parallel beam propagation and the spatial coherence of light coming from a third generation storage ring. The adaption of classical X-ray imaging schemes for synchrotron light sources has been developed since the late 1980s [1–4], which allowed for the method to be established during the 1990s [5–10], especially since sub-micrometre resolution became achievable [11]. The development introduced the use of contrast modes like inline phase contrast, holotomography, diffraction contrast, fluorescence contrast or analyzer-based imaging as standard techniques on synchrotron light sources (for a more detailed review see e.g. J. Banhart et al. [12]). To image dislocations and extended defects in single crystals by diffraction, white beam X-ray topography is applied [13]. Furthermore, imaging in two and three dimensions with high acquisition speed is performed [14–16] as well as scanning techniques combining different contrast modes [17]. Countless applications in diverse fields such as life science, materials research, archaeology, medicine, paleontology, non-destructive evaluation up to virtual material design have proved synchrotron-based micro-imaging to be a powerful tool (again, for a more detailed review see e.g. S. R. Stock [18, 19], J. Baruchel et al. [20, 21] or J. Banhart et al. [12]).

In this article we describe the micro-imaging instrumentation of the TopoTomo beamline at the ANKA facility in Karlsruhe, Germany. The beamline works with a peak photon flux density around 10^{11} ph/s/mm^2, assuming an energy bandwidth of around 1% as typically reached when employing multilayer monochromators. This moderate photon flux limits the performance compared to beamlines of other third generation light sources (with ring energies above 3 GeV), which offer a peak photon flux density of one or two orders of magnitude higher. Similar to the micro-imaging station at the BAM*line* (BESSY, Germany), we use several optimisation approaches in order to strengthen the performance of the set-up. This includes the use of different scintillator materials depending on the application or X-ray beam compression to increase the available photon flux density [22–24]. With an optimized detector concept, we achieve spatial resolution up to 2.5 μm for standard applications (effective pixel size < 1 μm). For selected applications like fast phase contrast radiography on living organisms a white beam mode delivers the required photon flux density. The spatial

resolution of the imaging set-ups will be brought substantially beyond the micrometer limit by using a Bragg magnifier in one or two dimensions. Absorption contrast [1, 25] and phase contrast [7, 26–28] transmission imaging as well as diffraction imaging techniques [29, 30] are available. An analyzer-based imaging device is under commissioning [31, 32]. Talbot interferometry is under development [33–37]. The combination of diffraction and transmission imaging methods at one beamline is beneficial for several industrial applications as well [38]. A co-operation with the Fraunhofer Institut für Techno- und Wirtschaftsmathematik (Kaiserslautern, Germany) is the basis for development and application of quantitative image analysis methods on three-dimensional volume data [39–43].

II. ANKA'S TOPOTOMO BEAMLINE

The German synchrotron light source ANKA (**An**gströmquelle **Ka**rlsruhe), a division of the Forschungszentrum Karlsruhe (Karlsruhe Research Centre – FZK) started operation by the end of the year 2000 with first user experiments in 2003 [44]. The 2.5 GeV storage ring delivers radiation for currently 14 beamlines (12 located at bending magnet ports, two insertion device beamlines, two additional insertion device beamlines are in the construction phase) [45]. The energy spectrum available at ANKA is suited for a vast variety of X-ray diffraction analysis and imaging methods. As a large scale facility of the Helmholtz Association of National Research Centres, ANKA is part of the German and European infrastructure offered to scientific and commercial users for performing excellent science and technological development. Commercial users have full access to professional services of the ANKA facility and the FZK infrastructure on a contractual basis via ANKA's Commercial Service department (ANKA COS) [38, 46].

The TopoTomo beamline currently hosts an experimental station for white beam X-ray topography and a new instrument for micro-radiography and micro-tomography. The beamline was formerly known as FLUO-TOPO [29, 47]. The X-ray fluorescence endstation was recently relocated to a separate, dedicated bending magnet source [48]. A few selected characteristics of the TopoTomo source and the ANKA storage ring are given in table I.

The micro-imaging station at TopoTomo and the present plus future beamline optics components optimized for imaging techniques are described in the following sections. Additionally, first successful imaging experiments are reported, including fast white beam phase

contrast micro-radiography and micro-tomography in absorption as well as white beam phase contrast.

A. Beamline layout

Figure 1 shows the layout of the TopoTomo beamline. Located on a standard ANKA bending magnet (1.5 T, bending radius 5.6 m), the beamline is currently exclusively operated in white-beam mode. A double-multilayer monochromator (DMM) optimized for full-field imaging will be installed in 2009 (see next section). The white-beam option will however remain accessible [48].

An assembly of removable attenuators on two motorized holders just downstream of the front end, at 8.5 m from the source, is available for spectral filtering of the beam. Figure 2 shows calculated spectra of the beam for typical attenuator settings.

With an electron beam size of 0.5 mm × 0.14 mm (horizontal × vertical, FWHM) for the bending magnets and emittance values (RMS) of 41 nm rad (horizontal) and 0.3 nm rad (vertical), the ANKA storage ring has characteristics that resemble second-generation installations. Moreover, due to the limited dimensions of the ANKA experimental hall, the beamline length of TopoTomo is limited to 32 m. Nonetheless, this beamline is well adapted to coherent full-field imaging due to its simple yet careful layout. The beamline is windowless except for the final exit window in the experimental hutch, 28 m from the source point. The only mandatory optical element in the beam path is thus the vacuum exit window, made of 0.5-mm-thick polished beryllium.

The transverse coherence length for X-ray photons of 20 keV (as defined by $l_c = \lambda z/s$, with λ the X-ray wavelength, z the distance from the source, and s the FWHM source size) is 4 μm (h) × 13 μm (v), which is sufficient for many methods using inline phase contrast, such as white-beam phase radiography and tomography [49]. For the quantitative reconstruction of phase-contrast tomography data of weakly absorbing samples, a simple but robust algorithm [50] was implemented.

For experiments that require a higher degree of transverse coherence in the horizontal or vertical direction, or for diagnostic purposes, a pair of slits is included in the front end, 4.8 m from the source point. For example, these slits can be used to obtain a horizontal coherence length that is equal to the vertical coherence length (with open slits), by closing the

horizontal slit gap to 0.12 mm (which reduces the available photon flux roughly proportional to the reduction of the source size). With these settings and using the maximum propagation distance of 1 m between sample and detector, up to 60 % of the phase contrast for a fully coherent beam can be obtained at 20 keV.[96] An example application is introduced in section IV A of this article.

Another set of high-quality in-vacuum slits is located just upstream of the vacuum exit window, 28 m from the source. This slit pair can also be used for white-beam section topography. The X-ray topography set-up and applications are described elsewhere [29, 30, 47]. Because this method needs classical X-ray film, a dark room is located nearby the experimental hutch.

B. Double-multilayer monochromator

The large amount of photons available at a synchrotron light source makes it possible to use X-ray monochromators, which reduces imaging artifacts and increases the contrast. Frequently, so-called multilayer monochromators are applied [51, 52] instead of crystal monochromators which are more common for synchrotron light sources. The reason is the larger spectral bandwidth of the reflection from a multilayer mirror in comparison to a Bragg crystal. As a result, the photon flux is increased by about two orders of magnitude when using a multilayer monochromator instead of a crystal monochromator [22, 23, 53–57].

The double-multilayer monochromator (DMM) for the TopoTomo beamline is fully designed and built by ACCEL Instruments GmbH (Germany). The concept is based on a DMM realized for the BAM*line* (BESSY) [22, 23, 58]. Here, each multilayer is placed on its own rotation axis. The two substrates deflect the beam vertically. Each multilayer mirror is equipped with a vertical stage for height adjustments allowing for compensation of varying incoming beam heights and giving a certain flexibility choosing the DMM offset. Furthermore, by moving the multilayers vertically out of the beam, a white beam option is available. The second multilayer can be moved in the beam direction by 700 mm in order to cover the energy range available at TopoTomo for X-ray micro-imaging. The installed system will allow one to work with a variable beam offset depending on the multilayers chosen. Due to the high requirements on stability the massive vacuum chamber will be mounted directly on a U-shaped granite block which guaranties efficient damping of floor vibrations. As there

is no front-end window for the TopoTomo beamline, strong vacuum design rules have to be followed. This includes that no vacuum grease is used. Therefore, only ceramic-bearing stages are applied inside the vacuum vessel. A water cooled fluorescence screen is installed at the downstream end of the vacuum vessel to monitor the white beam or the beam as reflected by the first and/or second multilayer. A sketch of the DMM design is presented in fig. 3. The key characteristics of the DMM system are summarized in the following:

- compact design, fully in vacuum
- totally free of water-to-vacuum joints
- high precision and backlash-free cross spring bearing based Bragg rotational stages
- integrated angular encoders on Bragg cradles
- upward-reflecting configuration
- stable and precise fixed-exit solution
- possibility for white-beam transport through the DMM system
- *in-situ* multilayer exchange by means of in vacuum horizontal stage setup
- roll adjustment unit for the 1st multilayer.

The multilayer coatings are deposited on 320 mm long substrates (300 mm optical length, 80 mm width) by AXO Dresden GmbH (Germany) [59]. The first of the two substrates is water-cooled from its sides. Each substrate contains two multilayer stripes (29 mm width), both with identical d-spacing and number of layers but different material composition. Different materials are necessary to avoid absorption edges of the coating material which otherwise could significantly reduce the available photon flux. Example calculations for the TopoTomo beamline assuming a W/Si coating (250 layers, 2.5 nm d-spacing) and a Mo/Si coating (250 layers, 2.5 nm d-spacing) can be found in fig. 4. A calculated photon flux density profile with the W/Si multilayers set to 10 keV photon energy is shown in fig. 5.

Much like in to the BAM*line* DMM, the second multilayer is bendable. The bending option allows for vertical beam collimation which can be used to increase the flux in absorption contrast imaging [23, 55].

III. IMAGING STATION

The micro-imaging station as pictured in figure 6 consists of two main components: the sample manipulator and a suitable indirect X-ray pixel detector. The manipulator uses a high precision horizontal linear stage to move the sample in and out of the beam in order to record reference images of the flat beam and to position the sample and rotation axis in the beam and relative to the detector. On top of this linear stage a high precision air bearing rotation stage provides the main axis for tomography scans (both high precision stages are by Micos GmbH, Germany). A cradle and a vertical translation stage (HUBER Diffraktionstechnik GmbH & Co. KG) are used for alignment. The complete manipulator set-up has been described in detail elsewhere [23]. Additionally, two linear stages with 300 mm travel range (Micos GmbH, Germany) were installed for X-ray topography of Si-wafers or radiography of larger objects [60].

For the high resolution X-ray pixel detector different indirect detecting systems are used. Indirect pixel area detectors for X-ray techniques have been applied successfully for several decades, starting in the 1970s with live topography [61]. During the 1990s the concept was successfully adopted for synchrotron-based micro-imaging and developed further to reach spatial resolutions in the sub-micrometre range [6, 11, 62]. Here, a scintillator screen (transparent single crystal or powder screen) is coupled via visible light microscope optics to a digital camera (CMOS or CCD). The maximum achievable resolution is determined by the numerical aperture of the microscope optics as well as the emission wavelength of the scintillator. Different scintillator materials, depending on the X-ray energy, the required field of view and the spatial resolution are applied [23, 63]. Additionally, ANKA is currently coordinating a European funded project – Scin^{TAX}, Sixth Framework Programme (STRP 033 427) – which aims at developing novel thin scintillators based on modified LSO (Lu_2SiO_5) crystals [64–66].

In order to optimize the performance of the indirect X-ray pixel detectors according to the individual experimental demands different optics, cameras and scintillator materials are combined. In this way, limitations introduced by the moderate photon flux density of the TopoTomo beamline can be partially compensated. Examples of detector-scintillator combinations frequently used are introduced in section III B (see as well tables II and III).

A. Microscope & macroscope concept

Similar to the BAM*line* (BESSY) two visible light optics have been installed in order to project the luminescent image of a scintillator onto a digital pixel detector [23]. For high spatial resolution, a commercially available microscope system by the French company Optique Peter (Lyon) is used, see fig. 6 (right) [67]. Its motorized revolving nosepiece holds three Olympus microscope objectives combined with a 2.5x eye-piece. They give access to magnifications from 3.125x to 50x (cf. table II) and spatial resolution up to the sub-micrometre range. Other motorized features of the detector microscope are the focus and the camera orientation. The high resolving power of the system is demonstrated in figure 7. For experiments requiring larger fields of view a so-called macroscope is used, see fig. 6 (left). It consists of low-magnifying Rodenstock objectives with large numerical apertures [68] as front objective and commercial tele-objectives as tube lens which results in a field of view of up to 24 mm x 16 mm (cf. table III). Glass filters can be placed in the beam path of visible light in order to block luminescence light coming e.g. from a scintillator's substrate which could deteriorate the resolution. An adaptable iris placed next to the glass filter is used to change the numerical aperture of the whole system, typically required when working with different cameras which commonly do not have the same intrinsic pixel size [23]. The system has proved to be very well suited for fast white beam cineradiography, in which radiographic images of live animals are taken at repetition rates of several hundred frames per second [69, 70]. Additionally, it can be applied for diffraction imaging techniques like X-ray topography. Here, one topograph for one selected diffraction vector can be recorded with the same high resolution as high resolution film [30, 60], but with shorter exposure time and increased dynamic range. A dedicated system for white beam synchrotron micro-imaging which resists the corresponding high heat load is currently in the production phase.

B. Scintillators

Concerning the scintillator screens an optimized concept based on known materials [63] was established where the screen used is selected by well-defined criteria in order maximize the performance [23]. Polished single crystal wafers with parallel surfaces are the first choice for luminescence screens in order to minimize blurring of the images by internal scattering of visible light. The remaining limiting factors for the resolution are the depth of focus

of the microscope optics (corresponds to their numerical aperture) used, the wavelength of maximum emission, and scattering of the X-rays inside the scintillator. Depending on the X-ray energy, the scintillator crystal has to be chosen with the maximal stopping power for minimal exposure times. The spatial resolution required defines the maximal thickness of the active layer of scintillation, the maximal polished area available determines the scintillator for moderate resolutions where larger objects are imaged. Finally the imaging speed has to be considered, e.g. minimal afterglow times are required for fast radiography. For moderate resolutions R $\geq$ 5 μm in combination with the macroscope frequently bulk CWO ($CdWO_4$) and LYSO:Ce (Ce doped (Lu, Y)$_2SiO_5$) crystals, polished by the FEE GmbH (Germany) as well as LuAG:Ce (Ce doped $Lu_3Al_5O_{12}$) (Crytur, Czech Republic) are used. For higher spatial resolution (between 2 μm and $<$ 5 μm) polished BGO ($Bi_4Ge_3O_{12}$) and CWO crystals, thinned down to 40 μm thickness and glued on top of a YAG ($Y_3Al_5O_{12}$) substrate, are applied in combination with the microscope (FEE GmbH) [23, 71–73]. Resolution better than 2 μm is achieved by thin LuAG:Eu crystals (5 μm, 10 μm and 25 μm thickness) grown on top of undoped YAG substrates by liquid phase epitaxy (CEA LETI, France and FEE GmbH, Germany), again combined with the microscope [11, 74]. Preliminary experiments with first novel LSO:Tb (Tb doped Lu_2SiO_5) crystals have shown a unique performance [64–66].

Commonly, at the moderate hard X-ray energies of the TopoTomo beamline the efficiency of the detector is mainly driven by the stopping power of the scintillator crystal applied, followed by the light collection efficiency of the optics and the efficiency of the camera sensor. While bulk heavy scintillator crystals (more than 100 μm thick, e.g. LuAG:Ce, CWO, LYSO:Ce) can easily reach for up to 100% stopping power at energies below 20 keV, the attenuation becomes a strongly limiting factor when going towards higher resolution in combination with thin scintillating crystal films. At 15 keV the 10 μm LuAG:Eu transmits approx. 60% of the X-ray photons, a 5 μm LuAG:Eu even more than 75%. Results of indirect detector efficiency measurements can be found in [62, 63, 66].

C. Cameras

The criteria for selecting a camera for synchrotron-based micro-imaging using indirect detection schemes are the read-out speed (typically a minimum of several frames per second

is required), dynamic range (full well capacity vs. read-out noise, a minimum of 12bit is required), quantum efficiency (should be at least 40% between 400 nm and 700 nm, to be able to apply a broad range of scintillator materials), small pixel size and a large chip (to be compatible with standard optics) [75]. Depending on the experimental demands different CCD and CMOS detectors are used for micro-imaging at the TopoTomo beamline. The performance of the cameras in the visible light regime is checked before installation by classical characterization schemes [76]:

- pco.4000 (PCO AG, Germany) – equipped with a Kodak KAI-11000 interline transfer CCD chip (4008 × 2672 pixels, each 9 μm in size), the maximum read-out speed at high dynamic range without region of interest or binning: 1.4 frames per second (a dynamic range of 5 000:1 was measured with exposure times between 0.1 s and 10 s) and 5 frames per second with reduced dynamic range, one signal unit (ADU) corresponds to a charge of 3 electrons in the corresponding potential well of the CCD chip, peak quantum efficiency above 50% at 500 nm, 4 GB on board memory are installed for fast data acquisition, for effective pixel sizes and fields of view see as well tables II and III [77],

- the European Synchrotron Radiation Facility (ESRF) in-house development FReLoN 2k14bit employs the E2V CCD chip TH7899M (2048 × 2048 pixels, each 14 μm in size), the maximum read-out speed at high dynamic range without region of interest or binning: >16 frames per second (a dynamic range of 13 800:1 was measured with an exposure time of 0.05 s), higher frame rates are achievable when running the camera in frame transfer mode or so-called kinetics pipeline mode, one signal unit (ADU) corresponds to a charge of 18 electrons in the corresponding potential well of the CCD chip, peak quantum efficiency above 40% around 700 nm, for effective pixel sizes and fields of view see as well table II [78],

- first experiments with a pco.1200hs CMOS camera for fast imaging have shown that image acquisition speeds of several hundred up to several thousands frames per second are achievable with white beam phase contrast micro-radiography (cineradiography) [15, 69, 70].

D. Bragg magnifier

Analyzer-based imaging (ABI) is a phase-sensitive imaging technique that utilizes Bragg reflection at an analyzer crystal between sample and detector as contrast mechanism [79]. Through refraction, the sample introduces angular deviations into the beam, which are then attenuated during reflection. In a geometrical optics approximation the observable intensity is proportional to the first derivative of the phase of the wave after transmission through the sample.

The highest achievable spatial resolution of standard x-ray imaging applications is slightly below 1 μm, limited by the detection systems available [11]. By using asymmetric Bragg reflection it is possible to magnify the x-ray image before detection and thus the achievable spatial resolution is improved significantly [31, 32]. Assuming the use of a commercial CCD-based X-ray camera for large field of view and high quantum efficiency with common pixel sizes in the order of few ten micrometre [75] and Bragg magnification factors of 100fold and above are easily accessible, the resulting spatial resolution is well in the sub-micrometre regime. The experimental set-up (refer to Fig. 8 for more details) of the so-called "Bragg Magnifier" consists of two analyzer crystals with perpendicular diffraction planes in order to provide two-dimensional magnification. An achieved spatial resolution of 0.4 μm was experimentally demonstrated at the beamline ID19 of the ESRF (France) [80], while an angular sensitivity, which directly relates to the sensitivity to density variations present in the sample, has been theoretically estimated to be in the order of micro-radians [81].

The standard post-detection procedure for quantitative analysis of images obtained by ABI with symmetric Bragg reflection is the so-called diffraction-enhanced imaging algorithm (DEI). With DEI it is possible to separate the contributions of absorption and (differential) phase contrast to the experimental images. Recently, this algorithm was extended to be suitable for the Bragg Magnifier and it proved to be well combinable with computed tomography [82].

The implementation of a Bragg Magnifier at the TopoTomo beamline is planned and the comparable moderate beam flux delivered by the bending magnet constitutes a challenge. Therefore, a double-crystal monochromator (DCM) with asymmetric Bragg reflections and beam compression will be used for increasing the flux. Since the field of view of the Bragg Magnifier is 2 mm x 2 mm at maximum, it is more advantageous to use a horizontal monochromator set-up because the beam can be compressed more strongly due to the

larger horizontal beam size (cf. table I). A compression factor of 7 is planned for the entire DCM resulting in a gain of flux in the same order. In the near future, test experiments will serve to demonstrate the feasibility of imaging with the Bragg Magnifier at the TopoTomo beamline.

IV. APPLICATIONS

Various experiments have been carried out since the separation of the former FLUO-TOPO beamline into FLUO and TopoTomo [29, 47]. These include white beam phase contrast tomography on mosquitoes [49], fast white beam phase contrast cineradiography on various living insects [69, 70] or digital white beam synchrotron topography to map stress and strain in large silicon wafers [30, 60].

A. Transmission imaging

An example of micro-tomography at the TopoTomo beamline for materials science applications is displayed in figure 9. The tomographic slice (upper left, absorption contrast mode) shows an injection mould green metallic micro part consisting of steel powder (6.5 μm mean particle size diameter, 63 vol-% powder loading). The aim of this study is to understand powder binder separations, a well known phenomenon in powder injection moulding (PIM). Due to the high surface to volume ratio in MicroPIM surface effects and also separation effects get more and more dominant. In this study, synchrotron micro-tomography and subsequent image analysis is used to measure local particle size distributions and local particle densities in samples produced by MicroPIM (specimens commonly have a quadratic cross section with an edge length of about 260 μm and an overall length of more than 3 mm) [83]. The volume data is tomographically reconstructed using the common filtered back projection algorithm [84] via the software package PyHST (ESRF) [85]. Quantitative volume image analysis is performed using the software package MAVI [39]. As an example, the local density distribution is calculated from a volume image consisting of 240 slices, see figure 9 (upper right).

White beam phase contrast micro-tomography is used at the TopoTomo beamline to image skeleton parts of marine organisms. In detail, the study looks at spicules forming the silica skeleton of marine sponges. In this way one hopes to resolve a number of questions, e.g.

the possibility of a spiral structure of the core with a characteristic "pitch". This could be a species specific structure or specific to a certain spicule type that may be found in a number of different sponge species. The skeleton gives the sponge its shape and general body plan. It also allows it to endure forces such as currents and waves [86]. By reducing the source size via TopoTomo's aperture slit system one can visualize the core of a spicule by means of white beam phase contrast imaging. An example radiograph is given in figure 10 (a) (0.9 μm pixel size, approx. 2.5 μm detector resolution, 25 μm thick LuAG:Eu single crystal, effective 10x magnification / 0.16 NA, 150 μm $\times$ 150 μm opening of the aperture slit system – at this resolution, closing the aperture slit increased the required exposure time from a few seconds to several tens of seconds). Figure 10 (b) shows a scanning electron microscope image of a spicule core, Figure 10 (c) a tomographic slice of a comparable sample. These tomographic images of the spicule's core allow for a characterization of its shape and size throughout the whole spicule. This will enable one to create a three-dimensional model of the spicule showing structural layers and internal as well as external details.

B. White beam synchrotron-based X-ray topography

Topography which uses a continuous X-ray spectrum is sensitive for short and long range strain in single crystals. The white beam synchrotron topography is based on recording a Laue-pattern of reflections where each reflection contains a topograph from the same investigated crystal position [13]. Depending on the crystal properties different techniques are applicable: Large area and section transmission topography image defects and strain of a large volume crystal slice. Back reflection and grazing incidence topography allow the analysis of defects in a certain depth of the sample which depends from the wavelength and the angle of incidence, respectively [29].

In a first example a large area transmission topograph of Bi-doped GaSb is shown in fig. 11 as an example for short range strain. The contrasts originate from different types of dislocations, stacking faults and dopant striations respectively. Corresponding to the [111] growth direction a 60^o network of misfit dislocations at the interface between the undoped seed and the Bi-doped crystal appear in the reflection. This reflection shows the projection of the (111) interface through the 0.8 mm thick crystal slice and was selected by tilting the crystal by 10^o relative to the incoming beam. Straight lines correspond to the threading

dislocations from the seed. As explained above, the straight lines are identified as 60^o dislocations of the type **b**=a/2<110>. It is clearly visible, that most of the dislocations originate from the seed crystal. The dark shadow at the interface indicates some strain as a result of a slightly different dopant concentration in the seed and grown crystal, respectively. In this area some new V-shaped dislocations are created and the dislocation density is analysed to be about 10 000 cm^{-2}. The horizontal lines correspond to dopant striations. In principle, crystals with dislocation densities of about 106 cm^{-2} can be characterised quantitatively (VRP-M high resolution film, 30 min exposure time).

Defects and strain in epitaxial layers and electronic devices can be imaged without distortions from the substrate using back reflection or grazing incidence geometries. Figure 12 compares the microscopic image (interference contrast microscopy, fig. 12a) and the back reflection topographs (figs. 12b and c) of a failed computer chip. No damage is visible in the light microscope even at higher magnification. As a result of strain the originally rectangular image is heavily deformed (lower right area) in the topographs. In addition the diffuse white and black contrast in the upper half of the 103 and 317 indicates the presence of strong long range strain. The absence of this contrast in other reflections is a sign of the anisotropy of the strain. In addition a series of internal strain fields become visible in the lower right corner with the maximum number for the 317 reflection. By comparing the number and positions in various reflections, information is gained about the geometrical position of such internal defects.

V. SUMMARY & OUTLOOK

In this article we introduced the micro-imaging facility at the TopoTomo beamline of the ANKA light source in Karlsruhe (Germany). The available X-ray micro-imaging systems are based on the use of scintillator crystals combined with diffraction limited microscope optics to magnify the luminescence image of the crystal onto the CCD or CMOS cameras. The TopoTomo beamline is equipped with different scintillator crystals and microscope optics, whose combination provides a broader range of spatial resolution values. The imaging set-up is completed by a high precision manipulator stage which controls the linear and the rotation movements of the specimen under analysis. Different X-ray imaging experiments are possible at the TopoTomo beamline, which include white beam phase contrast micro-

tomography and fast micro-radiography (cineradiography). In selected examples, imaging with absorption contrast is feasible as well.

The installation of an already constructed "Bragg magnifier" is in progress, which will allow for pushing the spatial resolution of the imaging set-ups beyond the micrometer limit. In addition, a double-multilayer monochromator will be installed which will both reduce the imaging artifacts and increase the contrast compared to white beam imaging. The commissioning of the Bragg magnifier and of the monochromator is foreseen for 2009. Afterwards the facility will be accessible for external users.

At present the TopoTomo beamline is exclusively operated in white-beam mode which makes it possible to perform white beam topography experiments. This beam option will remain available also after the installation of the monochromator.

Together with other imaging activities at ANKA, such as synchrotron computed laminography (for imaging flat extended samples) [87, 88], the development and production of refractive lenses fabricated by deep synchrotron radiation lithography [89, 90] and fluorescence imaging [47], a broad range of methods will be available for inhouse research within the Research Centre Karlsruhe as well as for external users.

Acknowledgments

We acknowledge T. Spangenberg, W. Mexner, H. Schade, R. Lang, V. Heger, R. Stricker, H. Heinzmann, R. Kleinschmidt, W. Möck, C. Frieh, K. Abel, D. Erbe, U. Herberger, M. Cholewa, P. Vagovic, D. Pelliccia, L. Helfen, A. Völcker, T. Fischböck, H. Waitz, A. Schult, J. König (FZK) for great support and suggestions, M. Klinger, T. Wolk (BAM), M. Bruno (KPE GmbH) for constructions and technical support, C. Maucher (Micos GmbH) for support with high precision stages, K. Dupré (FEE GmbH) for help with all the single crystals, C. Rau (Diamond), M. Stampanoni (SLS), S. Zabler, P. Zaslansky (MPG), F. De Carlo (APS), G. Weidemann, J. Goebbels, M. Hentschel, A. Lange, U. Zscherpel, W. Görner (BAM), F. Siewert (BESSY) for many fruitful discussions, W. Tutsch (PCO) for support with PCO cameras, A. Homs Puron, V. Rey Bakaikoa, J.-C. Labiche (ESRF) for support of the FReLoN.

[1] B. P. Flannery, H. W. Deckmann, W. G. Roberge, and K. L. D'Amico, Science **237**, 1439 (1987).

[2] P. Spanne and M. L. Rivers, Nucl. Instrum. & Meth. Phys. Res. B **24-25**, 1063 (1987).

[3] J. H. Kinney, Q. C. Johnson, M. C. Nichols, U. Bonse, R. A. Saroyan, R. Nusshardt, and R. Pahl, Rev. Sci. Instrum. **60**, 2471 (1989).

[4] W. Graeff and K. Engelke, in *Handbook on Synchrotron Radiation*, edited by S. Ebashi, M. Koch, and E. Rubenstein (North-Holland; Amsterdam, Oxford, New York, Tokyo, 1991), vol. 4, chap. Microradiography and Microtomography, pp. 361–406.

[5] A. Koch, Nucl. Instrum. & Meth. in Phys. Res. A **348**, 654 (1994).

[6] U. Bonse and F. Busch, Prog. Biophys. Molec. Biol. **65**, 133 (1996).

[7] P. Cloetens, R. Barrett, J. Baruchel, J.-P. Guigay, and M. Schlenker, J. phys. D, Appl. phys. **29**, 133 (1996).

[8] C. Raven, A. Snigirev, I. Snigireva, P. Spanne, A. Souvorov, and V. Kohn, Appl. Phys. Lett. **69**, 1826 (1996).

[9] H.-R. Lee, B. Lai, W. Yun, D. C. Mancini, and Z. Cai, in *Developments in X-ray Tomography*, edited by U. Bonse (1997), vol. 3149 of *Proc. of SPIE*, pp. 257–264.

[10] P. Spanne, C. Raven, I. Snigireva, and A. Snigirev, Phys. Med. Biol. **44**, 741 (1999).

[11] A. Koch, C. Raven, P. Spanne, and A. Snigirev, J. Opt. Soc. Am. **15**, 1940 (1998).

[12] J. Banhart, ed., *Advanced Tomographic Methods in Materials Research and Engineering* (Oxford University Press, 2008).

[13] T. Tuomi, K. Naukkarinen, and P. Rabe, phys. stat. sol. (a) **25**, 93 (1974).

[14] M. Di Michiel, J. M. Merino, D. Fernandez-Carreiras, T. Buslaps, V. Honkimäki, P. Falus, T. Martins, and O. Svensson, Rev. Sci. Instrum. **76**, 043702 (2005).

[15] F. García-Moreno, A. Rack, L. Helfen, T. Baumbach, S. Zabler, N. Babcsán, J. Banhart, T. Martin, C. Ponchut, and M. Di Michiel, Appl. Phys. Lett. **92**, 134104 (2008).

[16] A. Rack, F. García-Moreno, T. Baumbach, and J. Banhart, J. Synchrotron Radiat. **16**, in print (2009).

[17] P. Bleuet, E. Welcomme, E. Doorhyée, J. Susini, J.-L. Hodeau, and P. Walter, Nature Mater. **7**, 468 (2008).

[18] S. Stock, Int. Mater. Rev. **44**, 141 (1999).

[19] S. Stock, Int. Mater. Rev. **53**, 129 (2008).

[20] J. Baruchel, P. Cloetens, J. Härtwig, and M. Schlenker, in *Third-Generation Hard X-Ray Synchrotron Radiation Sources*, edited by D. M. Mills (John Wiley & Sons, Inc., New York, 2002), chap. Imaging with Third-Generation Synchrotron X-Rays, pp. 181–202.

[21] J. Baruchel, J.-Y. Buffiere, P. Cloetens, M. Di Michiel, E. Ferrie, W. Ludwig, E. Maire, and L. Salvo, Scripta Mater. **55**, 41 (2006).

[22] W. Görner, M. P. Hentschel, B. R. Müller, H. Riesemeier, M. Krumrey, G. Ulm, W. Diete, U. Klein, and R. Frahm., Nucl. Instrum. & Meth. in Phys. Res. A **467**, 703 (2001).

[23] A. Rack, S. Zabler, B. Müller, H. Riesemeier, G. Weidemann, A. Lange, J. Goebbels, M. Hentschel, and W. Görner, Nucl. Instrum. & Meth. in Phys. Res. A **586**, 327 (2008).

[24] A. Rack, H. Riesemeier, S. Zabler, T. Weitkamp, B. R. Müller, G. Weidemann, P. Modregger, J. Banhart, L. Helfen, A. N. Danilewsky, et al., in *Developments in X-ray Tomography VI*, edited by S. R. Stock (2008), vol. 7078 of *Proc. of SPIE*, pp. 70780X–1–70780X–8.

[25] P. Reimers and J. Goebbels, Mater. Evaluation **41**, 732 (1983).

[26] A. Snigirev, I. Snigireva, V. Kohn, and S. Kuznetsov, Rev. Sci. Instrum. **66**, 5486 (1995).

[27] K. A. Nugent, T. E. Gureyev, D. F. Cookson, D. Paganin, and Z. Barnea, Phys. Rev. Lett. **77**, 2961 (1996).

[28] A. G. Peele, F. De Carlo, P. J. McMahon, B. B. Dhal, and K. A. Nugent, Rev. Sci. Instrum. **76**, 083707 (2005).

[29] A. N. Danilewsky, R. Simon, A. Fauler, M. Fiederle, and K. W. Benz, Nucl. Instrum. & Meth. in Phys. Res. B **199**, 71 (2003).

[30] A. N. Danilewsky, A. Rack, J. Wittge, T. Weitkamp, R. Simon, H. Riesemeier, and T. Baumbach, Nucl. Instrum. & Meth. in Phys. Res. B **266**, 2035 (2008).

[31] W. J. Boettinger, H. E. Burdette, and M. Kuriyama, Rev. Sci. Instrum. **50**, 26 (1979).

[32] E. Förster, K. Goetz, and P. Zaumseil, Krist. Tech. **15**, 937 (1980).

[33] C. David, B. Nöhammer, H. H. Solak, and E. Ziegler, Appl. Phys. Lett. **81**, 3287 (2002).

[34] A. Momose, Jpn. J. Appl. Phys. **42**, L866 (2003).

[35] T. Weitkamp, A. Diaz, C. David, F. Pfeiffer, M. Stampanoni, P. Cloetens, and E. Ziegler, Opt. Express **13**, 6296 (2005), URL http://www.opticsexpress.org/abstract.cfm?URI=OPEX-13-16-6296.

[36] C. David, J. Bruder, T. Rohbeck, C. Grünzweig, C. Kottler, A. Diaz, O. Bunk, and F. Pfeiffer, Microelectron. Eng. **84**, 1172 (2007).

[37] E. Reznikova, J. Mohr, M. Börner, V. Nazmov, and P. J. Jakobs, Microsyst. Technol. **14**, 1683 (2008).

[38] A. Rack, L. Helfen, T. Weitkamp, A. Danilewsky, R. Simon, D. Lübbert, and T. Baumbach, in *AIP Conference Proceedings (CAARI2008)*, edited by F. Del McDaniel and B. L. Doyle (2009), vol. 1099, pp. 878–881.

[39] Fraunhofer ITWM, Department of Image Processing, *MAVI – modular algorithms for volume images*, http://www.itwm.fhg.de/mab/projects/MAVI/ (2009).

[40] M. Stiller, A. Rack, S. Zabler, J. Goebbels, O. Dalügge, S. Jonscher, and C. Knabe, BONE **44**, 619 (2009).

[41] A. Rack, L. Helfen, T. Baumbach, S. Kirste, J. Banhart, K. Schladitz, and J. Ohser, J. Microsc. **232**, 282 (2008).

[42] S. Zabler, A. Rueda, A. Rack, H. Riesemeier, P. Zaslansky, I. Manke, F. Garcia-Moreno, and J. Banhart, Acta Mater. **55**, 5045 (2007).

[43] S. Zabler, A. Rack, I. Manke, K. Thermann, J. Tiedemann, N. Harthill, and H. Riesemeier, J. Struct. Geol. **30**, 876 (2008).

[44] H. O. Moser, J. Alloy. Compd. **328**, 42 (2001).

[45] *The synchrotron light source ANKA*, http://ankaweb.fzk.de/ (last visit 2009).

[46] *ANKA Commercial Services (ANKA COS)*, http://www.anka-cos.de/ (last visit 2009).

[47] R. Simon, G. Buth, and M. Hagelstein, Nucl. Instrum. & Meth. in Phys. Res. B **199**, 554 (2003).

[48] *ANKA Instumentation Book*, http://ankaweb.fzk.de/downloads (last visit 2009).

[49] T. Weitkamp, A. Rack, D. Haas, T. Baumbach, D. Wegrzynek, E. Chinea-Cano, C. Streli, and P. Wobrauschek, in preparation (–).

[50] D. Paganin, S. C. Mayo, T. E. Gureyev, P. R. Miller, and S. W. Wilkins, J. Microsc. **206**, 33 (2002).

[51] P. Deschamps, P. Engstrom, S. Fiedler, C. Riekel, S. Wakatsuki, P. Hoghoj, and E. Ziegler, J. Synchrotron Radiat. **2**, 124 (1995).

[52] Y. S. Chu, C. Liu, D. C. Mancini, F. De Carlo, A. T. Macrander, B. Lai, and D. Shu, Rev. Sci. Instrum. **73**, 1485 (2002).

[53] P. Cloetens, W. Ludwig, J. Baruchel, D. V. Dyck, J. Landuyt, J. P. Guigay, and M. Schlenker, Appl. Phys. Lett. **75**, 2912 (1999).

[54] Y. Wang, F. De Carlo, D. C. Mancini, I. McNulty, B. Tieman, J. Bresnahan, I. Foster, J. Insley, P. Lange, G. Laszewski, et al., Rev. Sci. Instrum. **72**, 2062 (2001).

[55] Y. Wang, S. Narayanan, J. Liu, D. Shu, A. Mashayekhi, J. Qian, and J. Wang, J. Synchrotron Radiat. **14**, 138 (2007).

[56] M. Stampanoni, A. Groso, A. Isenegger, G. Mikuljan, Q. Chen, D. Meister, M. Lange, R. Betemps, S. Henein, and R. Abela, in *AIP Conference Proceedings (SRI2006)*, edited by J.-Y. Choi and S. Rah (2007), vol. 879, pp. 848–851.

[57] M. Störmer, C. Horstmann, D. Häussler, E. Spiecker, F. Siewert, F. Scholze, F. Hertlein, W. Jäger, and R. Bormann, in *Advances in X-Ray/EUV Optics and Components III*, edited by S. Goto, A. M. Khounsary, and C. Morawe (2008), vol. 7077 of *Proc. of SPIE*, pp. 707705–1–707705–9.

[58] H. Riesemeier, K. Ecker, W. Görner, B. R. Müller, M. Radtke, and M. Krumrey, X-Ray Spectrom. **34**, 160 (2005).

[59] R. Dietsch, T. Holz, D. Weißbach, and R. Scholz, Appl. Surf. Sci. **197–198**, 169 (2002).

[60] A. N. Danilewsky, J. Wittge, A. Rack, T. Weitkamp, R. Simon, and P. McNally, J. Mater. Sci.: Mater. Electron. **19**, 269 (2008).

[61] W. Hartmann, G. Markewitz, U. Rettenmaier, and H. J. Queisser, Appl. Phys. Lett. **27**, 308 (1975).

[62] H. Graafsma and T. Martin, in *Advanced Tomographic Methods in Materials Research and Engineering*, edited by J. Banhart (Oxford University Press, 2008).

[63] T. Martin and A. Koch, J. Synchrotron Radiat. **13**, 180 (2006).

[64] K. Dupré, M. Couchaud, T. Martin, and A. Rack, German Patent Application ref. no. DE 10 2007 054 700.7 (2007).

[65] *ScinTax – Novel ceramic thin scintillator for high resolution X-ray imaging*, http://www.scintax.eu (last visit 2009).

[66] T. Martin, P.-A. Douissard, M. Couchaud, A. Rack, A. Cecilia, T. Baumbach, and K. Dupré, IEEE Trans. Nucl. Sci., accepted for publication (2009).

[67] T. Weitkamp, C. Raven, and A. A. Snigirev, in *Developments in X-ray Tomography II*, edited by U. Bonse (1999), vol. 3722 of *Proc. of SPIE*, pp. 311–317.

[68] *Rodenstock – X-Ray Manual (catalogue) former Optische Werke G. Rodenstock – Precision Optics Division, now: Linos AG* (1992).

[69] O. Betz, A. Rack, C. Schmitt, A. Ershov, A. Dieterich, L. Körner, A. Ershov, and T. Baumbach, Synchrotron Radiat. News **21**, 34 (2008).

[70] A. Rack, F. García-Moreno, O. Betz, S. Zabler, C. Schmitt, T. dos Santos Rolo, A. Ershov, L. Helfen, J. Banhart, and T. Baumbach, IEEE Trans. Nucl. Sci., submitted for publication (2008).

[71] J. Touš, M. Horváth, L. Pína, K. Blažek, and B. Sopka, Nucl. Instrum. & Meth. Res. A **591**, 264 (2008).

[72] L. Nagornaya, G. Onyshchenko, E. Pirogov, N. Starzhinskiy, I. Tupitsyna, V. Ryzhikov, Y. Galich, Y. Vostretsov, S. Galkin, and E. Voronkin, Nucl. Instrum. & Meth. in Phys. Res. A **537**, 163 (2005).

[73] I. G. Valais, I. S. Kandarakis, A. Konstantinidis, D. N. Nikolopoulos, I. Sianoudis, D. A. Cavouras, N. Dimitropoulos, C. D. Nomicos, and G. S. Panayiotakis, Nucl. Instrum. & Meth. in Phys. Res. A **569**, 201 (2006).

[74] A. Koch, F. Peyrin, P. Heurtier, B. Ferrand, B. Chambaz, W. Ludwig, and M. Couchaud, in *Physics of Medical Imaging*, edited by J. M. Boone and J. T. Dobbins III (1999), vol. 3659 of *Proc. of SPIE*, pp. 170–179.

[75] S. M. Gruner, M. W. Tate, and E. F. Eikenberry, Rev. Sci. Instrum. **73**, 2815 (2002).

[76] J. Janesick, K. Klaasen, and T. Elliott, in *Solid State Imaging Arrays* (1986), vol. 570 of *Proc. of SPIE*, pp. 7–19.

[77] PCO AG / The Cooke Cooperation, *pco.4000 – cooled digital 14bit CCD camera system*, http://www.pco.de (last visit 2009).

[78] J.-C. Labiche, O. Mathon, S. Pascarelli, M. A. Newton, G. G. Ferre, C. Curfs, G. Vaughan, A. Homs, and D. F. Carreiras, Rev. Sci. Instrum. **78**, 0901301 (2007).

[79] D. Chapman, W. Thomlinson, R. E. Johnston, D. Washburn, E. Pisano, N. Gmur, Z. Zhong, R. Menk, F. Arfelli, and D. Sayers, Phys. Med. Biol. **42**, 2015 (1997).

[80] P. Modregger, D. Lübbert, P. Schäfer, and R. Köhler, phys. status. solidi A **204**, 2746 (2007).

[81] P. Modregger, D. Lübbert, P. Schäfer, and R. Köhler, Phys. Rev. B **74**, 054108 (2006).

[82] P. Modregger, D. Lübbert, P. Schäfer, and R. Köhler, Appl. Phys Lett. **90**, 193501 (2007).

[83] R. Heldele, S. Rath, L. Merz, R. Butzbach, M. Hagelstein, and J. Hauelt, Nucl. Instrum. &

Meth. in Phys. Res. B **246**, 211 (2006).

[84] A. C. Kak and M. Slaney, *Principles of Computerized Tomographic Imaging* (IEEE Press, New York, 1988).

[85] A. Mirone, R. Wilcke, A. Hammersley, and C. Ferrero, *PyHST – High Speed Tomographic Reconstruction*, http://www.esrf.eu/UsersAndScience/Experiments/TBS/SciSoft/ (last visit 2009).

[86] M. J. Uriz, X. Turon, M. A. Becerro, and G. Agell, Microsc. Res. Techniq. **62**, 279 (2003).

[87] L. Helfen, T. Baumbach, and P. Mikulík, Appl. Phys. Lett. **90**, 071915 (2005).

[88] L. Helfen, A. Myagotin, A. Rack, P. Pernot, P. Mikulík, M. Di Michiel, and T. Baumbach, phys. status. solidi A **204**, 2760 (2007).

[89] V. Nazmov, E. Reznikova, M. Boerner, J. Mohr, V. Saile, A. Snigirev, I. Snigireva, M. Di Michiel, M. Drakopoulos, R. Simon, et al., in *AIP Conference Proceedings (SRI2004)* (2004), vol. 705, pp. 752–755.

[90] E. Reznikova, T. Weitkamp, V. Nazmov, A. Last, M. Simon, and V. Saile, phys. status. solidi A **204**, 2811 (2007).

[91] A. Pogany, D. Gao, and S. W. Wilkins, Rev. Sci. Instrum. **68**, 2774 (1997).

[92] M. S. del Río and R. J. Dejus, in *Advances in Computational Methods for X-Ray and Neutron Optics*, edited by M. S. del Río (2004), vol. 5536 of *Proc. of SPIE*, pp. 171–174.

[93] S. Trabelsi Bauer, M. Bauer, R. Steininger, and T. Baumbach, Nucl. Instrum. & Meth. in Phys. Res. A **582**, 90 (2007).

[94] M. Born and E. Wolf, *Principles of Optics* (Cambridge University Press, 1999), 7th ed.

[95] C. E. Shannon and W. Weaver, *Mathematical Theory of Communication* (University of Illinois Press, 1963).

[96] This value was obtained for a phase modulation of 11 μm, which is the value of modulation period d for which $z = 1$ m is the optimum distance of the phase contrast transfer function [91] $C(z) = \sin(\pi\lambda z/d^2)$, for $\lambda = 0.062$ nm ($E = 20$ keV).

APPENDIX A: FIGURES

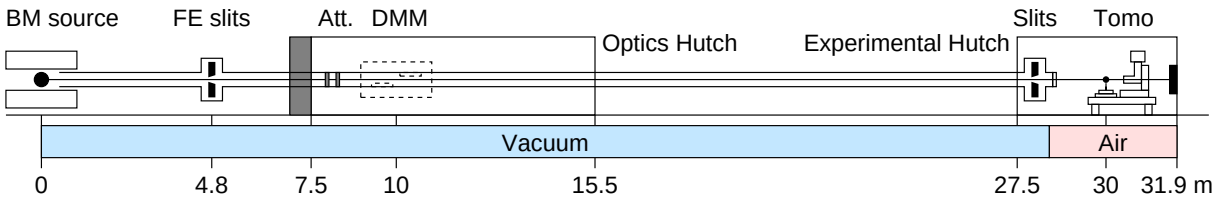

FIG. 1: (Color online) Layout of the TopoTomo beamline at the ANKA light source [48]. The beamline is windowless except for the final vacuum exit window in the experimental hutch (Be, 0.5 mm). From 2009 on a double-multilayer will be available with a fixed exit and a vertical focusing option. The white-beam mode will remain accessible.

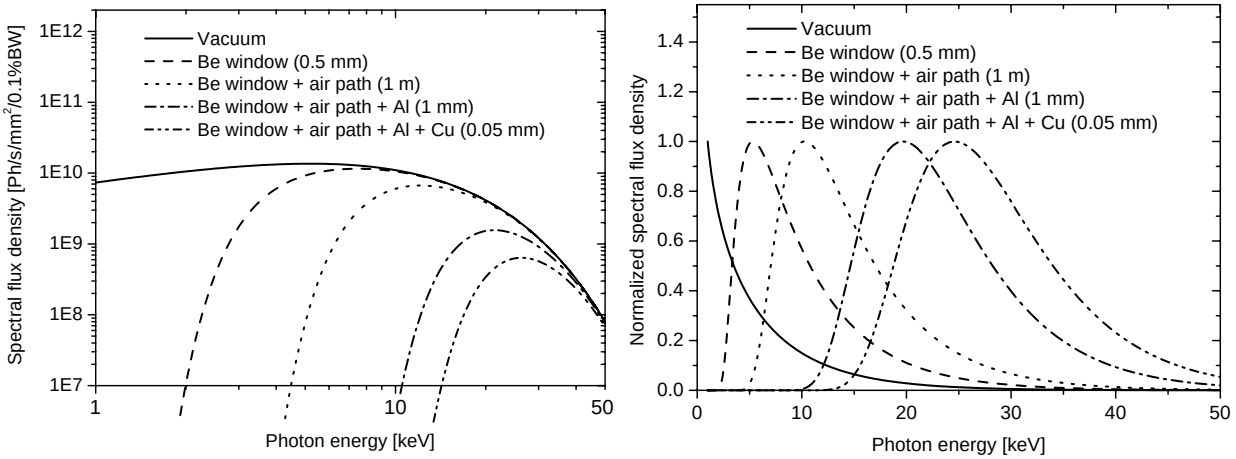

FIG. 2: Left: calculated energy spectrum of the X-ray beam at the TopoTomo beamline, for different combination of attenuating elements in the beam (100 mA ring current). Right: the same spectra with linear axis scaling, and with the flux normalized to a constant energy interval of 1 eV (the spectra for different filter settings have been normalized to their respective maximum values). Calculations made with XOP and DABAX database [92].

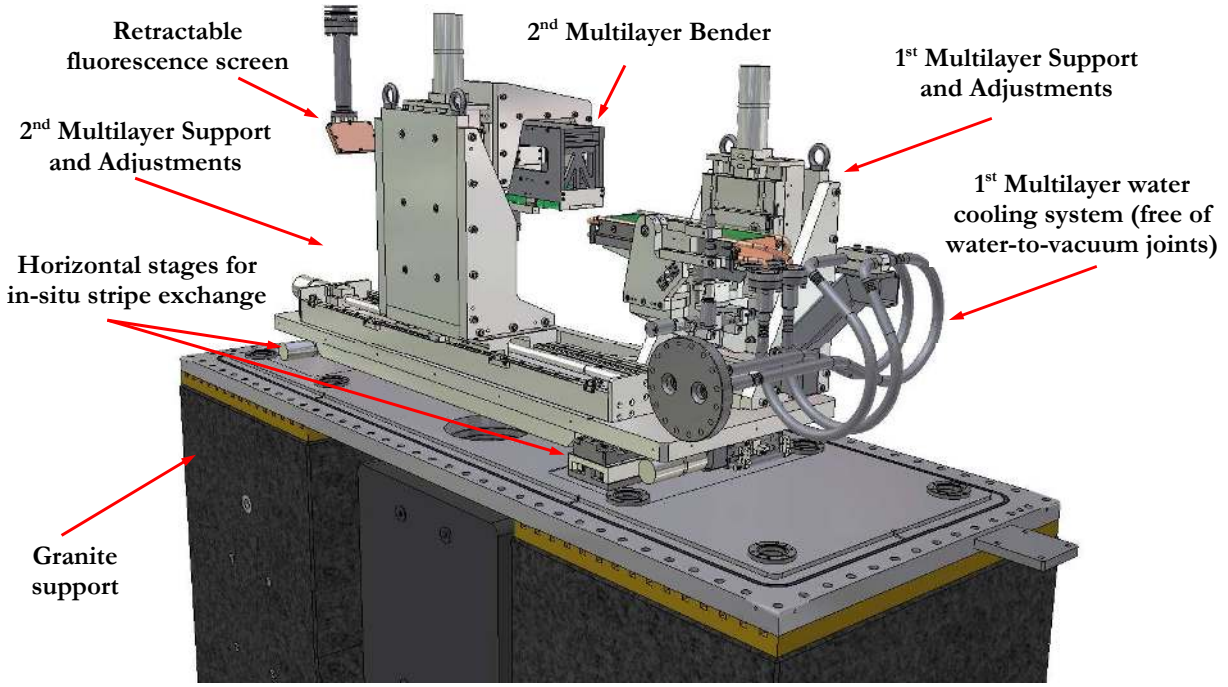

FIG. 3: (Color) Three-dimensional isometric view on the mechanical set-up of the DMM's optics assembly.

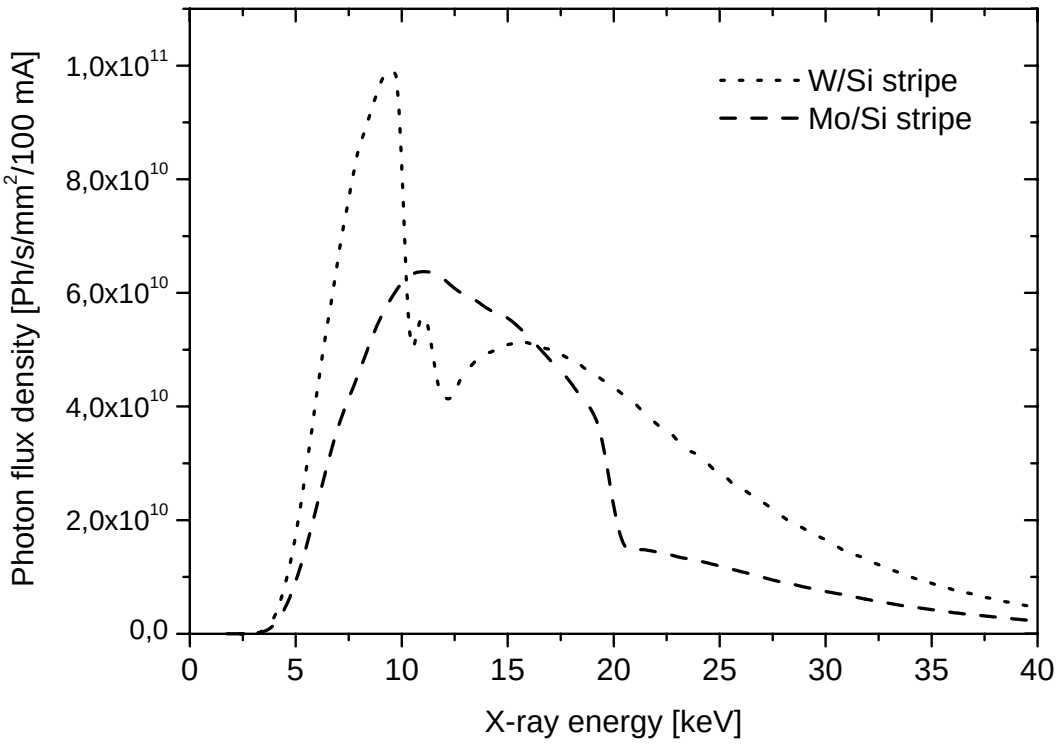

FIG. 4: Calculated photon flux densities within a 1 × 1 mm^2 pin-hole at the position of the TopoTomo experimental station when using the DMM (1% spectral bandwidth). The use of different material compositions (e. g. Mo/Si, W/Si, 250 layers, 2.5 nm d-spacing) allows one to avoid absorption edges of the coating materials. The calculations were made using XTrace [93].

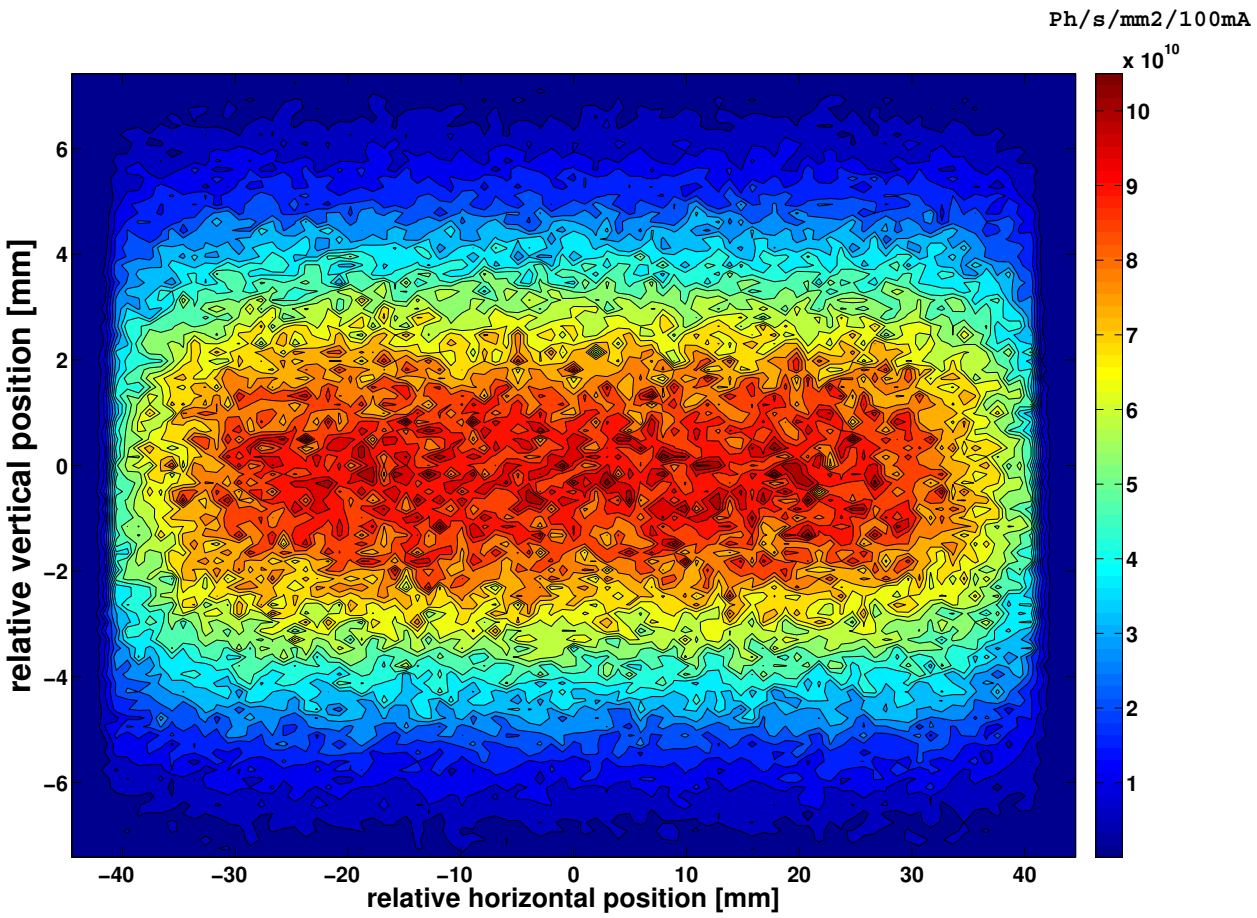

FIG. 5: (Color) The two-dimensional photon flux density profile of the TopoTomo beamline for an X-ray energy of 10 keV (100 mA ring current) at the position of the experiment (30 m distance to the source) when using the W/Si multilayer-coating of the DMM (250 layers, 2.5 nm d-spacing, cf. fig 4). The calculations were made using XTrace [93].

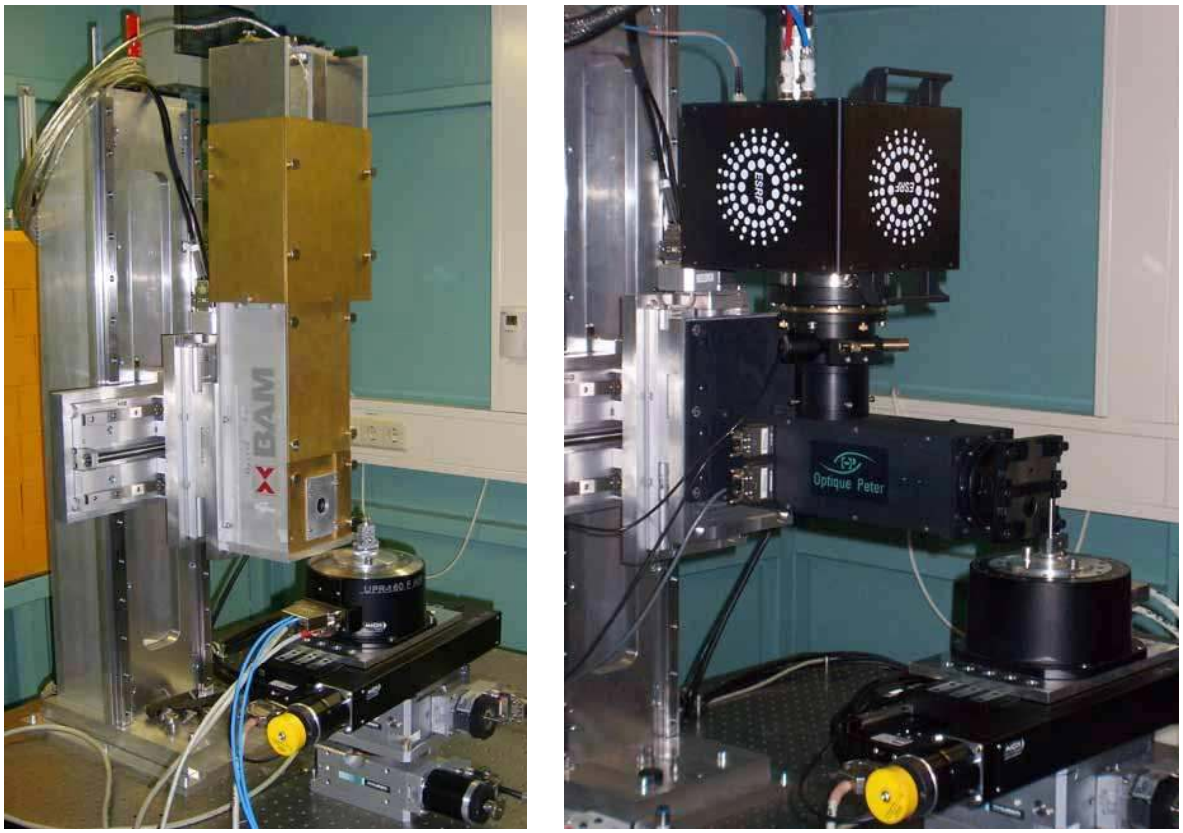

FIG. 6: (Color) Detector systems of the TopoTomo beamline mounted on xy-translation stages with a sample manipulator in front. Left: BAM*line* macroscope with pco.4000 CCD camera, right: OptiquePeter microscope with ESRF FReLoN 2k14bit [23, 67, 78].

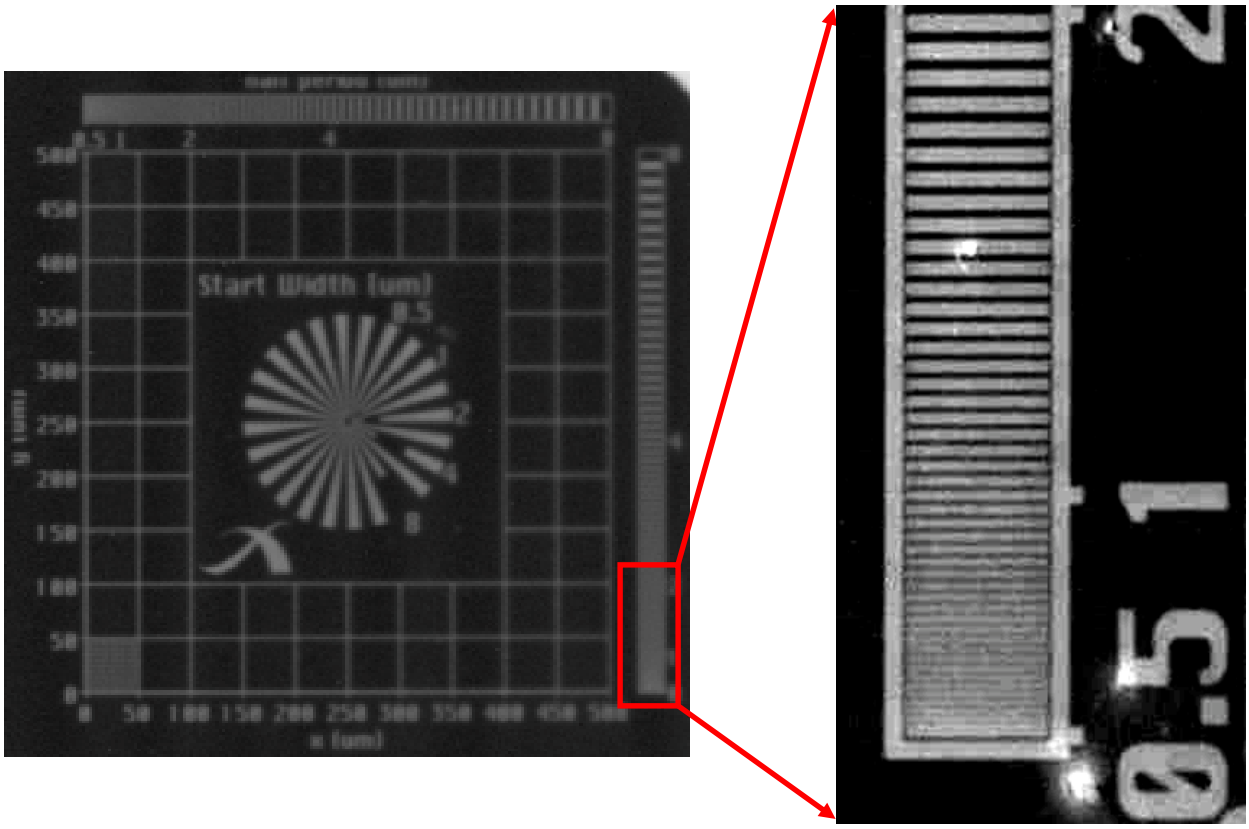

FIG. 7: (Color online) Left: overview image of a Xradia test pattern (X500-200-30) done at Topo-Tomo using the microscope (1.8 μm effective pixel size of, 40 μm thick CWO single crystal), right: vertical line pattern imaged with highest resolution (0.18 μm effective pixel size, 50x magnification / 0.75 NA microscope objective, LuAG:Eu scintillator 4 μm thick, white beam phase contrast).

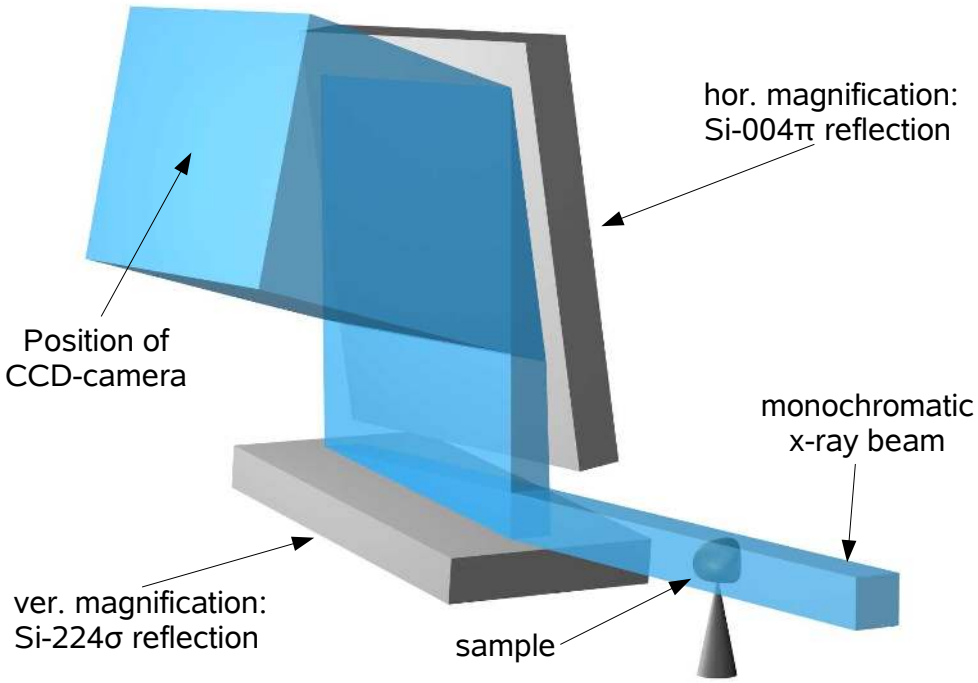

FIG. 8: (Color online) Schematic experimental set-up of the Bragg Magnifier. The contrast introduced by the sample is first vertically magnified by a Si-224 reflection and then horizontally by Si-004 reflection. The asymmetry of both reflections was chosen in order to provide 30–200fold magnification near the x-ray photon energy of 8.048 keV. More details can be found in [81].

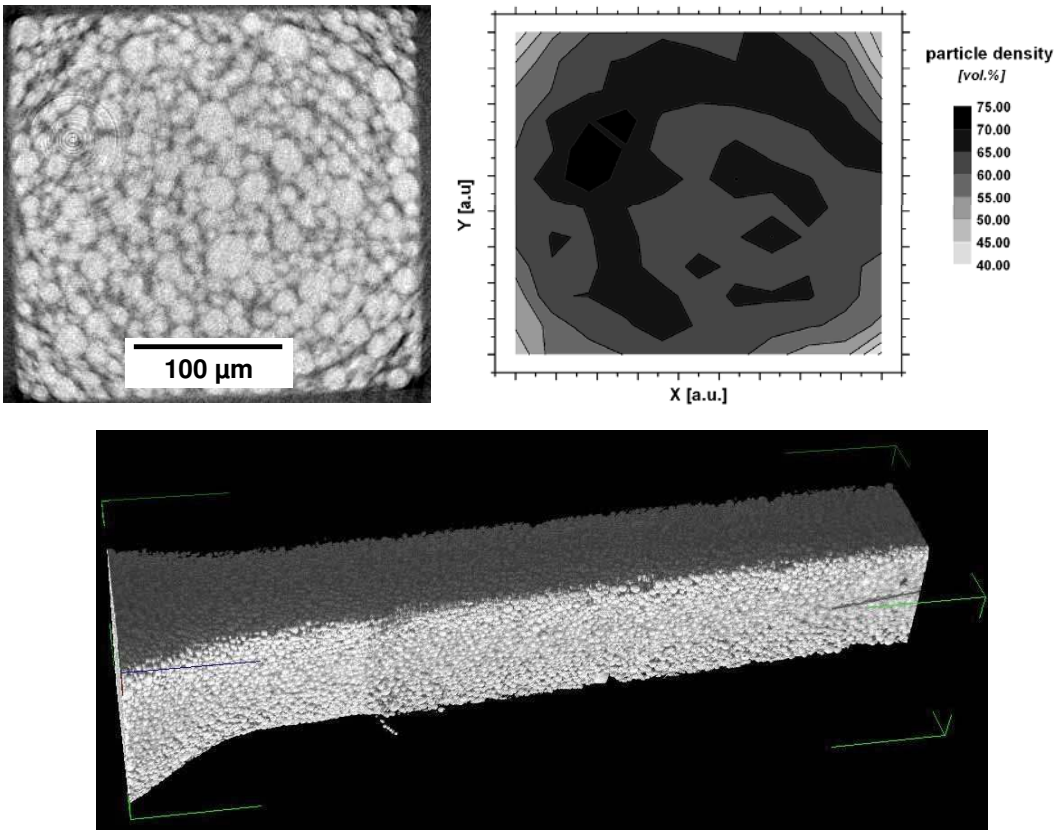

FIG. 9: Upper left: tomographic slice of an injection mould green metallic micro part consisting of steel powder [83] (∼2.5 μm spatial resolution / 0.9 μm pixel size, 25 μm thick LuAG:Eu single crystal, effective 10x magnification / 0.16 NA), bottom: corresponding volume rendering, upper right: local density distribution calculated from a volume image (Fraunhofer MAVI software [39]).

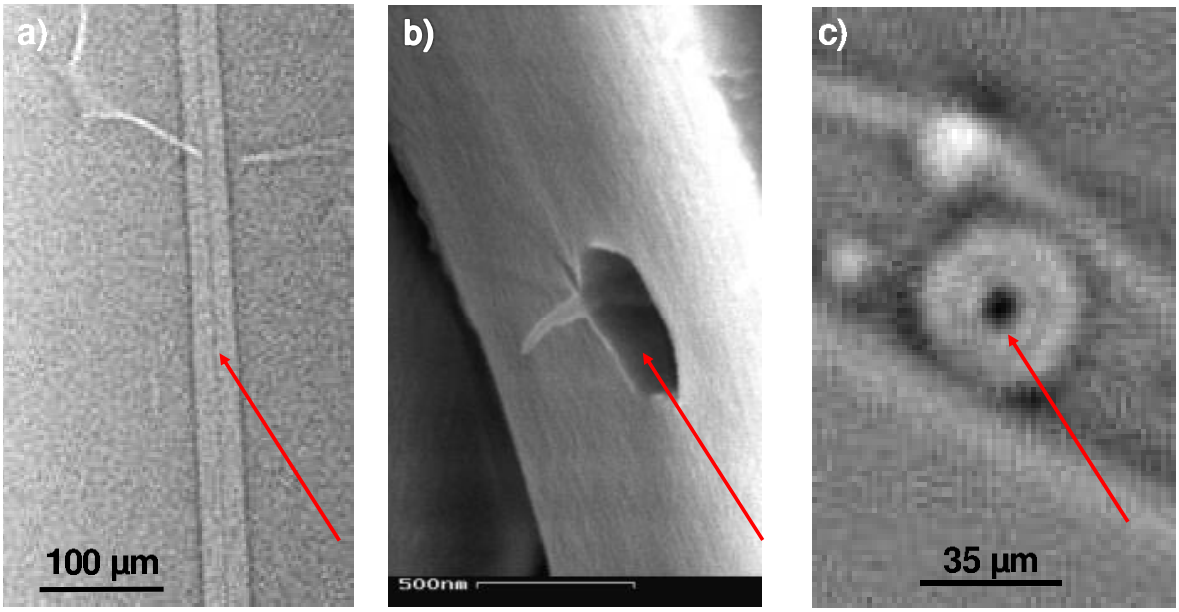

FIG. 10: (Color online) a) White beam phase contrast radiographic projection image showing spicule with core (0.9 μm pixel size, approx. 2.5 μm detector resolution, 25 μm thick LuAG:Eu single crystal, effective 10x magnification / 0.16 NA, 150 μm $\times$ 150 μm opening of the aperture slit system) b) scanning electron micrograph of a core of a sponge's spicule, c) tomographic slice of a comparable sample.

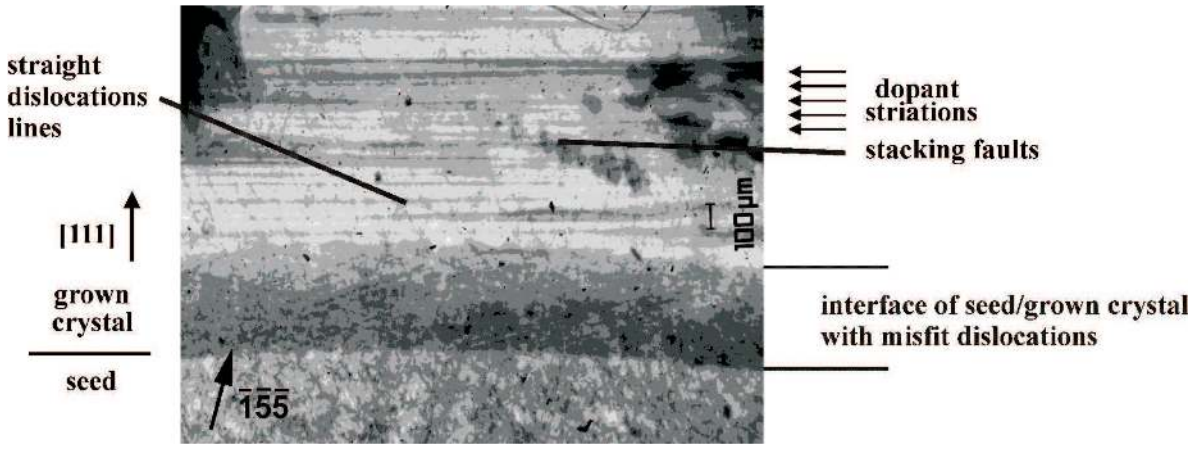

FIG. 11: Large area transmission topography of GaSb, Bi-doped, with a network of misfit dislocations, straight dislocations of the type **b**=a/2<110> and dopant striations.

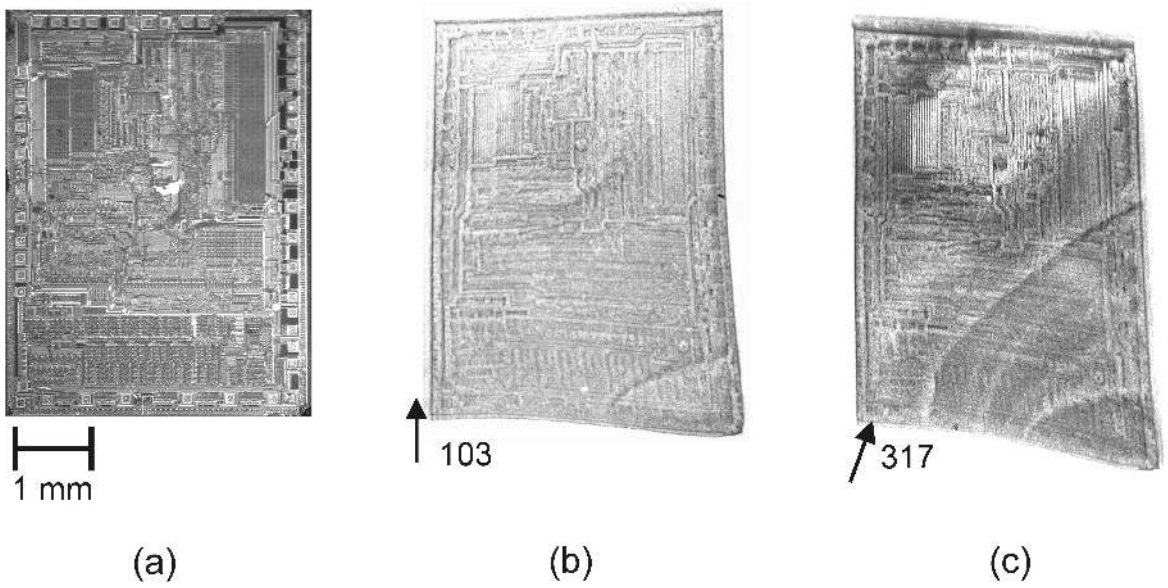

FIG. 12: Light microscopy (a) and large area back reflection topography (b) & (c) of a failed computer chip. (a): No defects are visible by interference contrast microscopy, (b) & (c): The bright circular contrast and the deformed reflections indicate anisotropic long range strain.

APPENDIX B: TABLES

Magnetic field (dipole)	1.5 T
Bending radius (dipole)	5.6 m
Critical photon energy	6.1 keV
Source size horizontal	0.50 mm (FWHM)
Source size vertical	0.14 mm (FWHM)
Maximum ring current	300 mA
Electron energy	2.5 GeV
Distance sample to source	30 m
Beam size at sample (white beam)	5 mm x 15 mm (V x H, FWHM)

TABLE I: Characteristics of ANKA's bending magnet beamline TopoTomo [48].

Objectives	Maximum Resolution FieldOfView FReLoN / PCO
Olympus *Plapon* 1.25x (NA = 0.04, 3.125x)	R > 7.6 μm 9.2 mm x 9.2 mm (4.5 μm) / 11.5 mm x 7.7 mm (2.9 μm)
Olympus *Plapon* 2x (NA = 0.08, 5x)	R > 3.8 μm 5.7 mm x 5.7 mm (2.8 μm) / 7.2 mm x 4.8 mm (1.8 μm)
Olympus *Uplsapo* 4x (NA = 0.16, 10x)	R > 3.1 μm 2.9 mm x 2.9 mm (1.4 μm) / 3.6 mm x 2.4 mm (0.9 μm)
Olympus *Uplsapo* 10x (NA = 0.40, 25x)	R > 0.8 μm 1.1 mm x 1.1 mm (0.6 μm) / 1.4 mm x 1.0 mm (0.4 μm)
Olympus *Uplsapo* 20x (NA = 0.75, 50x)	R > 0.4 μm 0.6 mm x 0.6 mm (0.3 μm) / 0.7 mm x 0.5 mm (0.2 μm)

TABLE II: Specifications of the OptiquePeter microscope optics, resulting maximum resolution R (Rayleigh criterion at 500 nm wavelength [94]), effective magnification (with a 2.5x eye-piece) and field of view (with effective pixel size in brackets) when applying the FReLoN 2k14bit CCD camera (2048x2048, 14 μm pixel size) or the pco.4000 (4008x2672, 9 μm pixel size).

Rodenstock Objective	Maximum Resolution FieldOfView
Rodenstock *TV-Heliflex* f = 50 mm, max. NA = 0.45, 3.6x	R > 5.0 μm (2.5 μm) 10.0 mm x 6.7 mm
Rodenstock *XR-Heliflex* f = 122 mm, max. NA = 0.40, 1.5x	R > 12.2 μm (6.1 μm) 24.4 mm x 16.3 mm

TABLE III: Specifications of the macroscope's Rodenstock optics, resulting maximum resolution R (Shannon's theorem [95]), magnification when employing a *Nikkor 180/2.8 ED* (f = 180 mm) as tube lens and field of view (effective pixel size in brackets) using a pco.4000 (the flexible iris of the macroscope allows one to trim the NA (maximum resolution) according to the effective pixel size).